Supporting information

Supraparticles on beads for supported catalytically active liquid metal solutions – the SCALMS suprabead concept

Thomas Zimmermann,[θ,a] Nnamdi Madubuko,[θ,b] Philipp Groppe,[θ,a] Theodor Raczka,[a] Nils Dünninger,[a,b] Nicola Taccardi,[b] Simon Carl,[c] Benjamin Apeleo Zubiri,[c] Erdmann Spiecker,[c] Peter Wasserscheid,[b,d,e] Karl Mandel,[a,f] Marco Haumann,*[,b,g] Susanne Wintzheimer*[,a,f]

a Department of Chemistry and Pharmacy, Inorganic Chemistry, Friedrich-Alexander Universität Erlangen-Nürnberg, Egerlandstrasse 1, D91058 Erlangen, Germany.

b Lehrstuhl für Chemische Reaktionstechnik (CRT), Friedrich-Alexander-Universität Erlangen-Nürnberg, Egerlandstrasse 3, D91058 Erlangen, Germany.

c Institute of Micro- and Nanostructure Research (IMN) & Center for Nanoanalysis and Electron Microscopy (CENEM), Interdisciplinary Center for Nanostructured Films (IZNF), Department of Materials Science and Engineering, Friedrich-Alexander-Universität Erlangen-Nürnberg, Cauerstrasse 3, D91058 Erlangen, Deutschland

d Erlangen Catalysis Resource Center and Interdisciplinary Center for Interface-Controlled Processes, Friedrich-Alexander-Universität Erlangen-Nürnberg, D91058 Erlangen, Germany

e Forschungszentrum Jülich, "Helmholtz-Institute Erlangen-Nürnberg for Renewable Energies" (IEK 11), Egerlandstr. 3, 91058 Erlangen, Germany

f Fraunhofer-Institute for Silicate Research ISC, Neunerplatz 2, D97082 Würzburg, Germany

g Research Centre for Synthesis and Catalysis, Department of Chemistry, University of Johannesburg, P.O. Box 524, Auckland Park 2006, South Africa.

* susanne.wintzheimer@fau.de, marco.haumann@fau.de

Experimental section

Chemicals: Köstrosol© KS2040 (CKW Chemiewerke Bad Köstritz GmbH), aluminium-tri-sec-butoxide (97%; Sigma-Aldrich), triethanolamin (97%; Sigma-Aldrich), water (deionized before use), isopropanol (99.8; Jäkle Chemie), ACCU® SPHERE SA 52238 (Saint-Gobain NorPro), gallium (99.9999%; Alfa Aesar), and dihydrogen hexachloroplatinate (IV) hexahydrate (99.5%; Alfa Aesar) were used without further purification.

Preparation of Ga-nanoparticle dispersion: The Ga nanoparticle dispersion was prepared by ultrasonication method. Using a rosette cell, 1g of gallium nugget (5N, Alpha Aeaser) was dispersed in 100 mL of isopropanol by ultrasonication (Branson – 450D sonifier). The sonifier was operated at 80% of maximum power for 30 min. at 40°C. After ultrasonication, the entire gallium dispersion was centrifuged at 8000 rpm for 10 min (HERMLE Labortechnik centrifuge Z 366). The supernatant is decanted and the sediment containing the Ga nanoparticles are used for the supraparticle fabrication.

Supraparticle fabrication: SPs were prepared in a toolbox-like approach using spray-drying as an assembly tool. In the first step, a defined amount of Ga nanoparticles was mixed with three times the mass of silica nanoparticles adjusting a theoretical Ga:SiO_2 mass ratio of 1:3. In the second step the particle mixture was diluted with deionized water to reach a final mass concentration of 20 wt%. The resulting mixture was sonicated using an ultrasonic bath (RK 514, Bandelin) for at least 10 min. The prepared nanoparticle mixture was then spray-dried to SPs using a Spray-Drier B-290 Mini (Büchi Labortechnik GmbH). The inlet temperature was set to 100 °C, with an aspirator power of 80 %, a carrier gas flow of 473 l/h, and a feed rate of 4.5 ml/min. The dispersion was stirred during spray-drying to avoid any sedimentation of particles over time. After spray-drying, the obtained SP powder was put into a muffle furnace LT5/11/B410 (Nabertherm GmbH) for

calcination. The temperature was set to 500 °C with a heating rate of 60 °C/h and held at 500 °C for 2 h.

Addition of active metal: The catalytically active metal was introduced into the fabricated Ga/SiO_2 SP by a galvanic displacement reaction as shown in Equation 1. A Ga/Pt molar ratio of 80 was targeted. For this, the actual gallium loading on the SP was determined by inductively coupled plasma atomic emission spectroscopy (ICP-AES). The Ga/SiO_2 SP was dispersed in 50 ml of isopropanol. An exact volume of the $H_2[PtCl_6] \cdot 6\ H_2O$(aq.) precursor solution ($c_{precursor}$ = 4.4 $mg_{Pt}\ mL^{-1}$) was added to the suspension. After 5 minutes of stirring, the solvent was slowly removed in a rotary evaporator at 40 °C and then calcined under air at 500 °C for 3 h. The Pt loading of the final catalyst was analysed by ICP-AES. The ICP-AES data can be found in the Table S1.

$$4Ga^0 + 3Pt^{4+} \longrightarrow 4Ga^{3+} + 3Pt^0 \quad (1)$$

Suprabead fabrication: Alumina beads (ACCU® SPHERE SA 52238) were washed three times with isopropanol, and dried at 120°C for 1 h. Afterward, they were stored in an exicator till usage. Alumatran was synthesized after,[R1] freed from solvent at 40 mbar and 90°C, and stored at -18°C till usage. The binder was prepared as a 50 wt-% solution of alumatran in ethanol via stirring at room temperature. 1g of beads are mixed for 2.5 minutes with 600 mg of the binder. Covered beads are transferred rapidly into prepared beds of supraparticles (320 mg) in 10 ml glass vials. Mixing started immediately after contact with the supraparticle bed and was done for at least 30 seconds. The supraparticle-covered beads are freed from unfixed supraparticles via sieving over a 125 µm nylon sieve. For calcination the sample is put into a muffle furnace LT5/11/B410 (Nabertherm GmbH) and heated up to 600 °C with a heating ramp of 2.5 K/min, hold at 600 °C for 4 h and cool down with a maximal cooling ramp of 2.5 K/min.

Reference material preparation: The reference materials used in this study were Ga-SBeads and Pt-SBeads. The Ga-SBeads was prepared using a similar approach described above for the GaPt-SBeads catalyst. However, in the Ga-SBeads catalyst, the addition of active metal was deliberately omitted to obtain an active metal free catalyst. On the other hand, the Pt-SBeads material was prepared by means of wet chemical impregnation. A Ga free SiO_2 SP was prepared using the spraydrying approach described under supraparticle fabrication. The prepared SiO_2 SP was dispersed in 50 ml of isopropanol and the exact amount of the $H_2[PtCl_6] \cdot 6\ H_2O$(aq.) precursor solution ($c_{precursor}$ = 4.4 $mg_{Pt}\ mL^{-1}$) was added to the suspension. After 5 minutes of stirring, the solvent was slowly removed in a rotary evaporator at 40 °C and then calcined under air at 500 °C for 3 h. The prepared Pt-SP was used for the suprabead fabrication as discussed earlier. In a final step, the formed Pt-SBeads were pretreated under a reductive atmosphere of hydrogen to reduce the Pt^{4+} into Pt^0. Details of the pretreatment conditions are described under the section "Propane dehydrogenation in a fixed bed tubular reactor". The metal loading of the final catalysts were analysed by ICP-AES. The ICP-AES data for both reference material can be found in the Table S1.

N_2-sorption measurements to determine surface area and pore size: Nitrogen isotherms were performed on a NOVAtouch LX2 (AntonPaar) at 77 K. Before measurements, the samples were dried at 30 mbar at 115 °C for 16 h in a vacuum drying chamber (VO29, Mammert) and degassed at 350 °C for 12 h under vacuum.

Electron microscopy: Transmission electron microscopy of silica nanoparticles (KS2040) was conducted on an LEO 912 Omega (Zeiss) using an acceleration voltage of 80 kV. Scanning electron microscopy (SEM) was performed on a JSM F-100 (JEOL). Topographic analysis was performed via secondary electron detection (2 kV accelerating voltage). Material contrast analysis was performed via back-scattered electron detection (6-8 kV accelerating voltage). Supraparticle-based

samples were sputtered with Pt before SEM analysis (except for SEM-EDX samples). For energy-dispersive X-ray spectroscopy the samples were prepared on conductive carbon pads and the accelerating voltage was set to 15 kV.

Cross-section preparation of supraparticles: For supraparticle cross-section analysis, supraparticle powder was attached to a conductive carbon pad and embedded between two silicon wafers. Cutting of cross-sections was performed on an IB-19530CP (JEOL) by using an Argon (Ar) plasma beam for 10h in pulse mode (40 s on, 20 s off). The Ar flow was set to 2,5 sccm and the accelerating voltage to 8 kV.

Cross-section preparation and imaging of suprabeads: For SBead cross-section analysis, a single SBead was attached to a conductive carbon pad. The cutting of the cross section was achieved by a laser ablation milling process utilizing the 3D-Micromac microPREP™ PRO laser ablation system (0.150 W, 20 kHz pulse frequency, 20 µm spot diameter, 1 µm pulse distance). The attained cross section was further cleaned by focused ion-beam (Ga+) milling utilizing the FEI Helios NanoLab 660 SEM/FIB Dual Beam system (30 keV acceleration voltage with 42 nA, 0.8 nA & 0.24 nA subsequently). Secondary electron (SE) and backscattered electron (BSE) imaging was performed using 2 keV, 0.4 nA (SE) and 5 keV, 0.8 nA (BSE).

In a second cross-section preparation approach (mechanical cross-section polish), single SBeads were embedded in a mixture of epoxy resin (EpoThinTM 2, Bühler (203440032)) and copper powder (70-CU0029, ~50 µm particle size, Micro to Nano). The embedded SBeads were milled down with SiC abrasive foil (P1200, P2400 and P4000 subsequently), polished with Al2O3 polishing powder and carbon coated (15 nm) with Leica EMACE 200 Carbon Coater.

Nano X-ray computed tomography (nano-CT): The nano-CT experiment was performed with a ZEISS Xradia 810 Ultra laboratory-scale X-ray microscope equipped with a 5.4 keV rotating anode

Cr source and a Zernike phase ring for phase contrast (PC) imaging. The supraparticle powder prepared as in the supraparticle fabrication procedure was transferred to the tip of a stainless steel tomography needle. For this, the dry particle powder was first distributed on a glass plate and then subsequently the tomography needle covered with UV light-sensitive adhesive (UHU BOOSTER LED Light®; UH48150) was carefully brought into contact with the dispersed particles on the glass surface, so that a small amount of the supraparticle powder stuck to the tip of the needle.

After that, the 180° nano-CT tilt series (721 projections with 0.25° tilt increment) was acquired in the high resolution phase contrast mode (HRES PC, 16 µm x 16 µm field of view, 50 nm spatial resolution) of the microscope with an illumination time of 170 s/frame. The tilt series was recorded in the native ZEISS microscope software (XMController and Scout&Scan). For the alignment of the tilt series the Active Motion Compensation (AMC; based on Wang et al.[R2] procedure implemented in the natives ZEISS software (XMController) was utilized. The final 3D reconstruction was performed using a simultaneous iterative reconstruction technique (SIRT) algorithm[R3] (150 iterations) implemented as an in-house Python script based on the Astra Toolbox.[R4] The final visualization of the results (Figure S2 and ESI† **Videos 1-3)** was performed using the Arivis Vision4D software.

Dynamic light scattering measurements: Hydrodynamic size measurements of Silica nanoparticles were performed via dynamic light scattering using a Zetasizer Nano (Malvern Panalytical) at 25 °C in deionized water. The shown data is averaged from three measurements with 11 individual runs each.

Laser diffraction measurements: Particle size measurements in volume size distribution of supraparticles were performed via laser diffraction measurements using a MICROTRAC S3500

Model Bluewave (Microtrac) with a Small Volume Sample Dispersion Unit Model DIF2022 (Malvern Instruments Limited).

Metal content analysis: The Ga and Pt loadings of the prepared reference and SCALMS catalysts was determined by inductively coupled plasma atomic emission spectroscopy (ICP-AES) using a Ciros CCD (Spectro Analytical Instruments GmbH). The solid samples were digested with concentrated HCl:HNO_3:HF (attention: HF is a dangerous compound, relevant safety precautions must be taken) in a 3:1:1 volumetric ratio, using microwave heating to 220 °C for 40 min. The instrument was calibrated for Pt (214.123 nm) and Ga (417.206 nm) with standard solutions of the elements before the analyses.

Propane dehydrogenation in a fixed bed tubular reactor: A defined catalyst mass of 3 g was placed into the fixed-bed reactor (quartz glass). The reactor was heated to the set point of 550 °C at 10 °C min^{-1} under an inert atmosphere of 100 mL_N min^{-1} argon. Due to the oxophilic nature of gallium, the presence of a thin passivating Ga_2O_3 layer has been reported on gallium-based materials.[R5,R6] The removal of this passivation layer can be facilitated in the presence of a noble metal under reductive conditions.[R6] For this reason, the catalysts were pretreated under the reductive atmosphere of 19.5 mL_N min^{-1} hydrogen as feed gas diluted with 80.5 mL_N min^{-1} argon. After a purge stream of 100 mL_N min^{-1} of argon for 60 minutes, the reaction was started by supplying 8.9 mL_N min^{-1} propane as feed gas diluted with 89 mL_N min^{-1} argon. The gas hourly space velocity (GHSV) was set at 1960 mL_{gas} $g_{Cat.bed}^{-1}$ h^{-1} under reaction conditions. The gases were dosed by mass flow controllers (MFC, Bronckhorst). All parts exposed to reagents, except for the fixed bed quartz reactor, were made of stainless steel type 1.4571. A tubular split furnace heated the quartz glass fixed-bed reactor. All reactor tubes and pipes outside the furnace were held at 100 °C by using heating tapes and fiberglass tape insolation.

Online analysis of reaction products: The product gas mixture was analyzed using online gas chromatography (GC) on a Bruker 456 GC equipped with a GC-Gaspro column (30 m x 0.320 mm) having, a thermal conductivity detector (TCD) for detecting the light compounds (H_2, Ar, He) and a flame ionization detector (FID) for detecting the C_1-C_3 hydrocarbons. The sample time for peak identification and resolving was 9.25 min.

The peak area obtained from the GC data was used in calculating the mole fraction (x) of each substance. The conversion for propane ($X_{propane}$) was calculated based on the molar balance of propane in the inlet ($x_{propane,in}$) and outlet ($x_{propane,in}$) of the reactor as described using Equation 2.

$$X_{propane} = \frac{x_{propane,in} - x_{propane,out}}{x_{propane,in}} \qquad (2)$$

The selectivity for the desired product propene ($S_{propene}$) was calculated based on the mole fraction of propene ($x_{propene}$) relative to the sum of the mole fraction of other side products namely methane, ethane, and ethene as described in Equation 3.

$$S_{propene} = \frac{x_{propene}}{x_{propene} + x_{methane} + x_{ethane} + x_{ethene}} \qquad (3)$$

The productivity of the catalyst was calculated for direct comparison between the activity of Ga_{130}Pt-SBead-1 and Ga_{45}Pt SCALMS. The productivity was obtained by dividing the mass flow of the desired product by the mass of the active metal Pt used during PDH ($m_{active\ metal}$) as described in Equation 4.

$$Productivity = \frac{\dot{m}_{propane} \cdot S_{propene} \cdot X_{propane}}{m_{active\ metal}} \qquad (4)$$

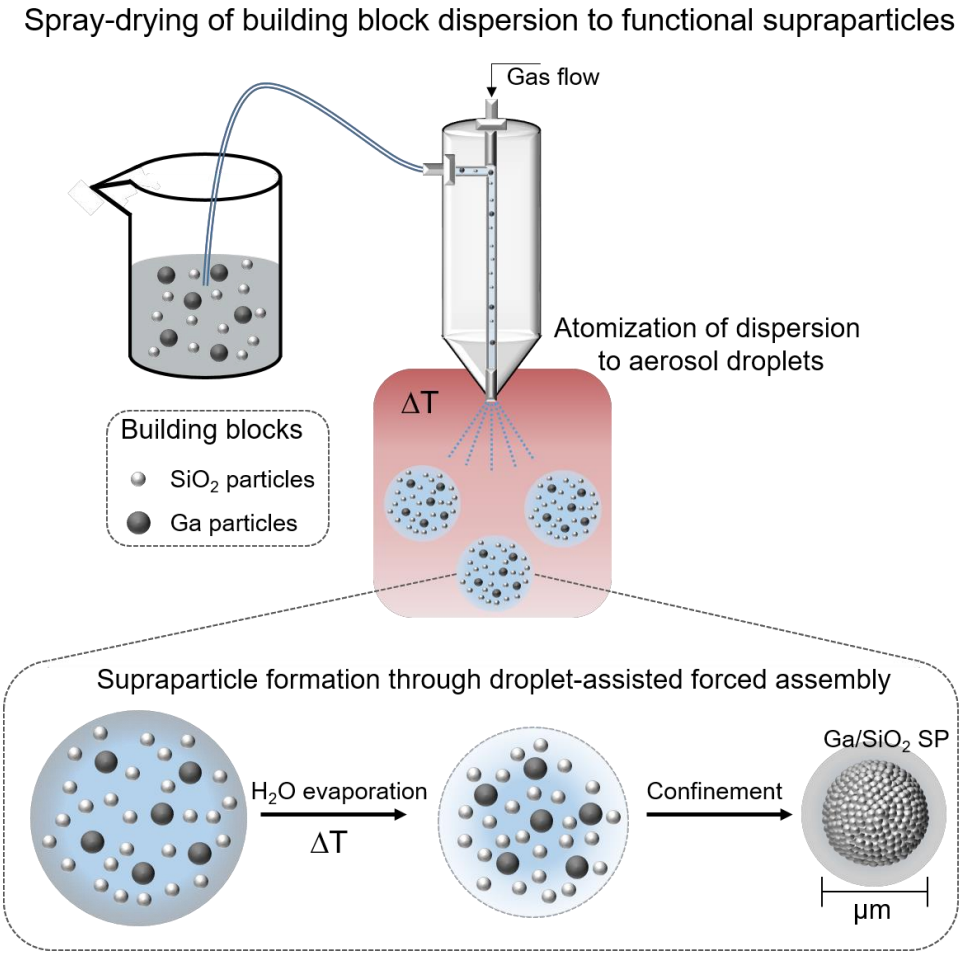

Figure S1: Scheme showing the spray-drying process of a silica and gallium nanoparticle dispersion and the forced assembly of the nanoparticles during droplet evaporation resulting in supraparticles. While there is a vast variety of synthesis methods for the creation of supraparticles, spray-drying is very popular due to its high flexibility in terms of the combination of different nanoparticle types (be it support or catalyst materials) and excellent upscalability. In this high-throughput method, aerosol droplets of nanoparticle dispersions are created by a nozzle and sprayed into a hot zone by a gas flow, initiating the drying process. Upon solvent evaporation, a droplet-assisted forced assembly of the contained nanoparticles into complex densely packed microscale supraparticles takes place. Usually, such entities exhibit a spherical morphology that resembles a raspberry. The obtained supraparticles are then collected, e.g., with the help of a cyclone as solvent-free powder. Their final composition, porosity, and morphology can be precisely tuned by varying process parameters and nanoparticle precursors.[R7,R8] The assembly of two types of nanoparticles via spray-drying has already been described in models and supported by experiments.[R9,R10]

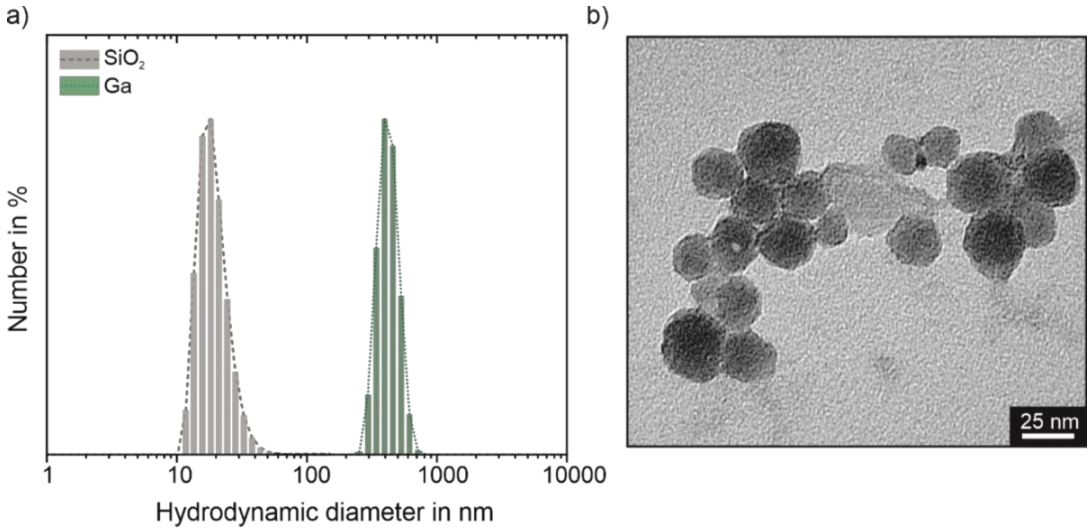

Figure S2: a) Dynamic light scattering measurements of silica nanoparticles and gallium droplets/nanoparticles and b) TEM of the utilized silica nanoparticles.. The mean hydrodynamic size distribution for silica nanoparticles was found to be 18 nm and for gallium droplets/nanoparticles to be 396 nm. The measured polydispersity index was measured to be 0.15 for the silica, and 0.68 for the gallium dispersion.

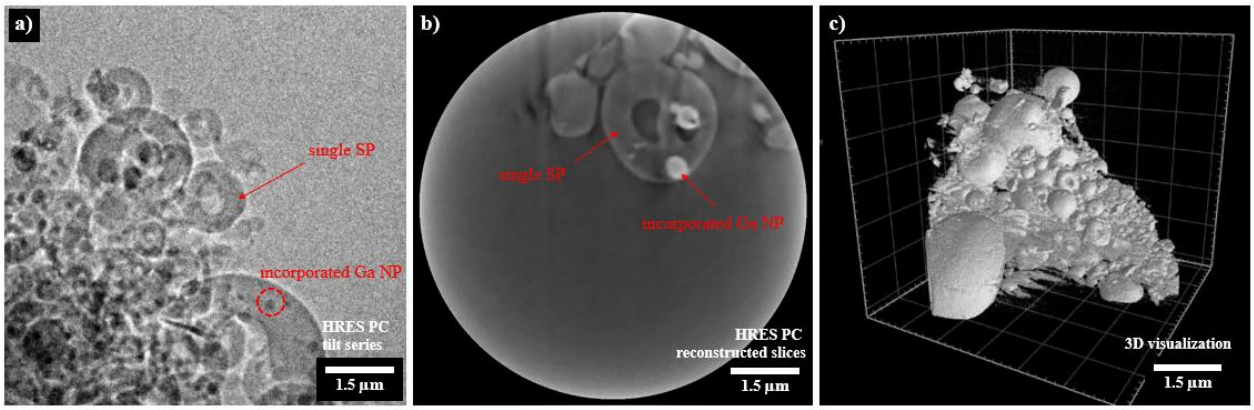

Figure S3: a) Single nano-CT projection in HRES PC mode showing an agglomeration of as prepared supraparticles on a tomography needle tip in projection. The higher absorbing Ga NPs appear as dark spots incorporated in the partially hollow and donut shaped supraparticles. b) Virtual slice through the HRES PC reconstruction, showing the hollow morphology of a single supraparticle and incorporated Ga NPs (bright in the

relative to a) inversed contrast). c) 3D visualization of the HRES PC nano-CT tilt series (by Arivis Vision 4D). The full videos can be found in ESI† **Video 1-3** respectively.

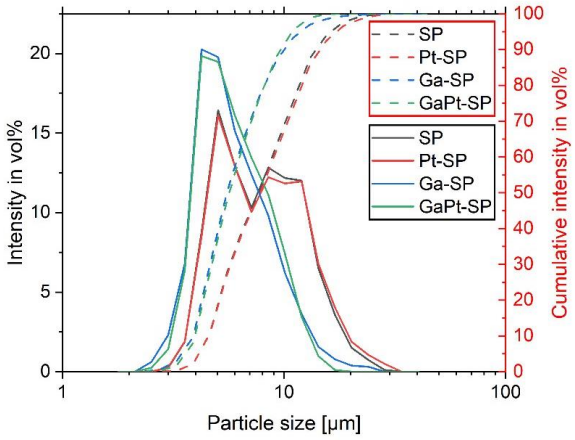

Figure S4: Particle size distribution in volume distribution obtained from laser diffraction measurements of synthesized supraparticles, showing that the supraparticles samples consisting of pure silica nanoparticles (SP; 4.57 µm d_{10}; 7.71 µm d_{50}; 13.78 µm d_{90}) and the platinum-loaded ones (Pt-SP; 4.58 µm d_{10}; 7.81 µm d_{50}; 14.41 µm d_{90}) possess a similar bimodal size distribution. Supraparticles sprayed with gallium (Ga-SP; 3.90 µm d_{10}; 5.51 µm d_{50}; 9.94 µm d_{90}) and their platinum-loaded counterparts (Ga_{130}Pt-SP; 3.97 µm d_{10}; 5.65 µm d_{50}; 9.61 µm d_{90}) also display a similar, but monomodal size distribution.

Table S1: Metal loading of Ga_{130}Pt-SBeads, Ga_{130}Pt-SP and for the reference materials Ga-SBead and Pt-SBead as determined from ICP-AES.

Sample name	Ga content in sample / wt%	Pt content in sample / wt%	Ga to Pt molar ratio / -
Ga_{130}Pt-SBead-1	1.69	0.04	128
Ga_{130}Pt-SBead-2	1.08	0.02	132
Ga_{130}Pt-SBead-3	0.85	0.02	142
Ga-SBead	2.36	0	-
Pt-SBead	0	0.08	-
Ga_{45}Pt-SCALMS[a]	3.01	0.19	45
Ga_{130}Pt-SP-1	22.29	0.80	78
Ga_{130}Pt-SP-2&3	26.05	0.60	124
Ga-SP	22.29	0	-
Pt-SP	0	2.30	-

[a] reference for conventional SCALMS materials (Fig. S14)

Determination of SP content within SBeads

The mass of the unfixed SP separated from the SBeads by sieving was determined. By subtracting this mass from the total mass of used SP the amount of SP fixed to the SBeads is obtained. The total mass of the SBeads were determined as the sum of the masses of alumina beads used, the solid content of the used binder and fixed SP. The weight percent of SP in SBeads was calculated as the ratio of mass from fixed SP to the total mass of SBeads (Table S2).

Table S2: SP loading of SBeads as calculated from used and obtained masses.

Sample name	Mass of SP fixed on bead / mg	Mass of total SBead / mg	SP content in SBead / wt%
Ga_{130}Pt-SBead-1	145.3	1450.4	10.0
Ga_{130}Pt-SBead-2	137.3	1441.7	9.5
Ga_{130}Pt-SBead-3	128.3	1431.6	9.0
Ga-SBead	166.8	1469.9	11.3
Pt-SBead	235.4	1542.9	15.3

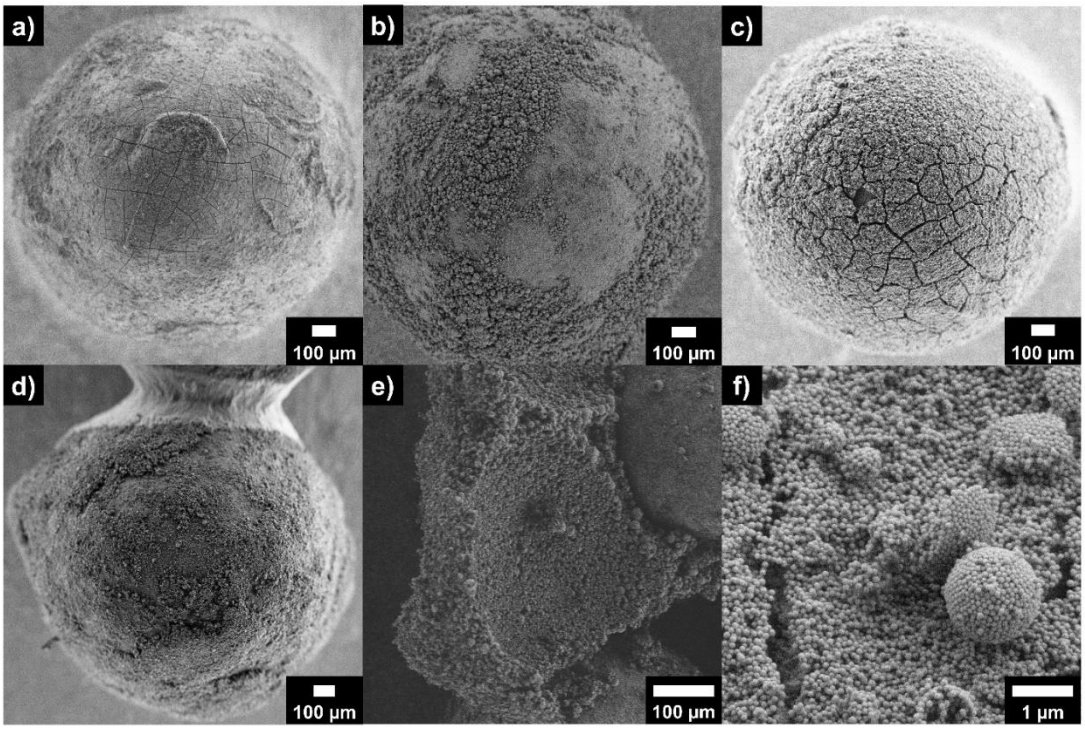

Figure S5: SEM of failed suprabead preparation attempts. a) Next to no supraparticles are bound to the core and cracks can be seen in the binder when the mixing time of the binder and beads is set too long and the binder dried up before coming in contact with the supraparticles. b) No complete coverage of the core with supraparticles is achieved when the used supraparticles are too large in diameter compared to the low amount of utilized binder and have fallen off due to insufficient fixation. c) Cracks in the supraparticles as well as the binder layer are caused by different thermal material expansions when too steep heating and cooling ramps are set for the heat treatment. d) Non-uniform coverage and the aggregation of large supraparticle-binder-clumps are the results of too high amounts of binder. e) Large supraparticle-binder-aggregates as well as insufficient core coverage is caused when mixing core, binder, and supraparticle at once. f) Insufficient supraparticle-binder contact and broken supraparticles are the results of using supraparticles with low mechanical stability.

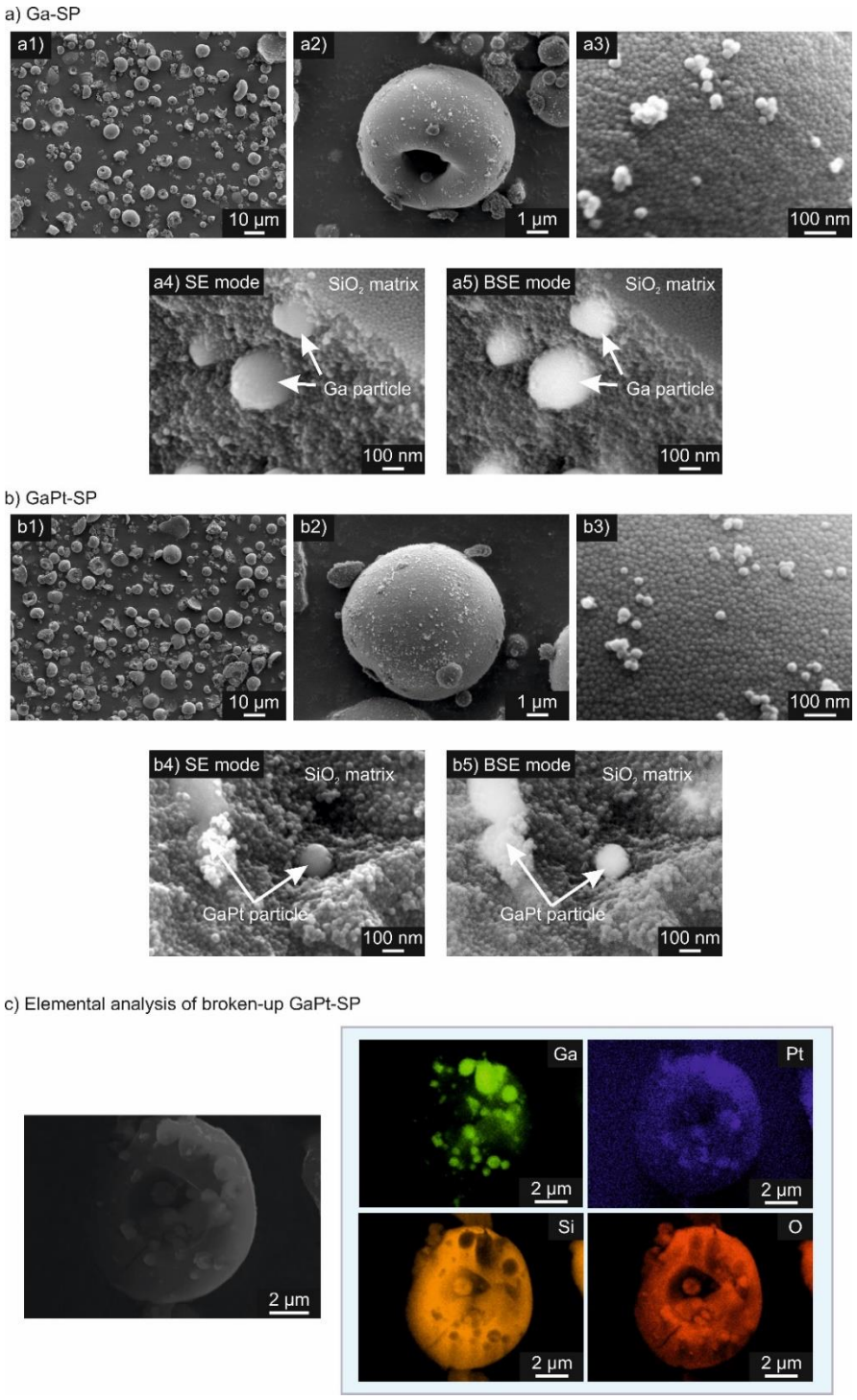

Figure S6: SEM of a) Ga-SP and b) $Pt_{130}Ga$-SP, with increasing magnifications from a1 to a3, and b1 to b3, respectively. Broken-up supraparticles in (a4, b4) SE and (a5, b5) BSE mode indicate that gallium nanoparticles are enclosed by silica nanoparticles within a supraparticle. EDS elemental mapping of GaPt-SPs (c) showing the distribution of Ga, Pt, Si, and O of a broken-up SP.

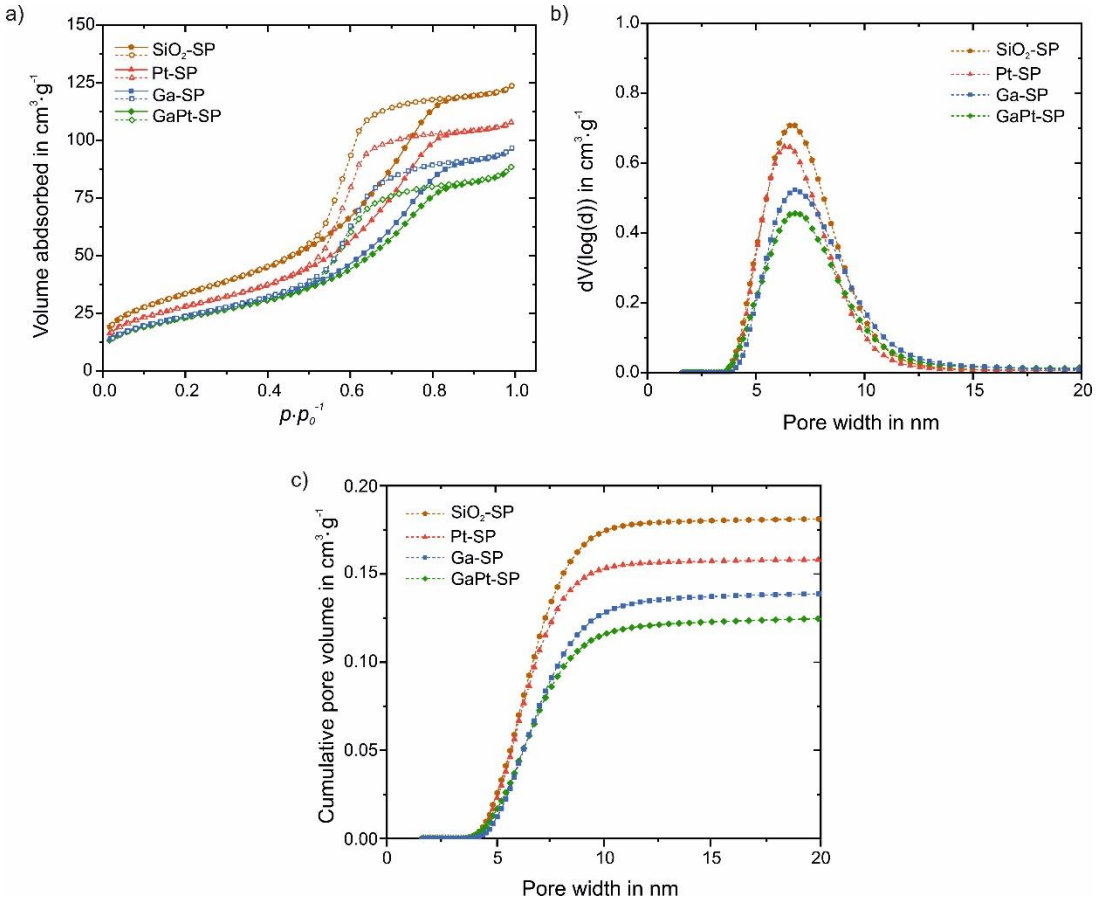

Figure S7: Pore system characterization of synthesized SPs with varying composition of building blocks via N_2 sorption at 77 K. a) N_2 isotherms; full symbols represent the adsorption branch and empty symbols the desorption branch. b) Pore size distribution obtained by non-local density function theory (NLDFT). c) Cumulative pore volume as a function of pore width.

The synthesized SPs feature type IV shaped isotherms independently of their building block composition which is characteristic for mesoporous materials that show pore condensation accompanied by hysteresis (type H2 hysteresis loop,[R11] Figure S7a)). The present hysteresis types indicate pore restrictions in the SP frameworks leading to pore blocking effects during N_2 desorption.[R11] The typical type IV saturation plateau extending above relative pressures ($p \cdot p_0^{-1}$) of 0.8 is clearly visible for all samples. This saturation indicates complete pore filling allowing the calculation of the total pore volume V_{pore} from the plateau region (Table S3). Furthermore, from the isotherms it is obvious that with varying SP composition the maximum N_2 uptake changes. This indicates changes in the overall accessible pore volume of the SPs when introducing Ga and/or Pt into the SiO_2 framework. By applying the NLDFT method to the adsorption branch (assumption: cylindrical pore shape) the pore size distribution and the cumulative pore volume can be calculated.[R12,R13] In combination with the N_2 isotherms this shows that the mesoporous character of the SPs is just minorly affected (Figure S7b and S7c). For all sample the pore distribution spans from approx. 4 nm to approx. 14 nm with a mean pore size d_{pore} between 6-7 nm. However, the cumulative pore volume shows a shifted pore volume increase to slightly higher pore widths for the Ga-containing samples which results in the slightly higher mean pore width of 6.8 nm. This is possibly due to the larger size of the Ga particles that are embedded into the SiO_2 framework decreasing the overall accessible pore volume and shifting the mean pore width to higher values. The specific surface area S_{BET} of all samples was obtained by applying the multi-point Brunauer-Emmett-Teller (BET) method in the $p \cdot p_0^{-1}$ range of 0.1 to 0.3.[R11]

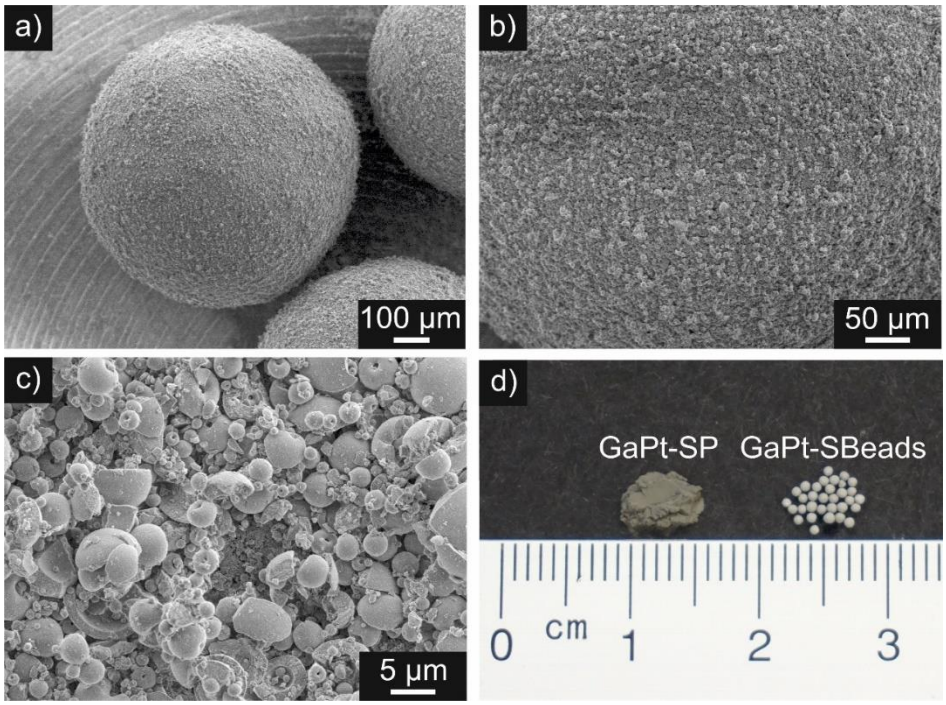

Figure S8: SEM of Ga_{130}Pt-SBead, with increasing magnifications from a) to c), and a photograph of Ga_{130}Pt-SPs, as well as G_{130}aPt-SBeads d).

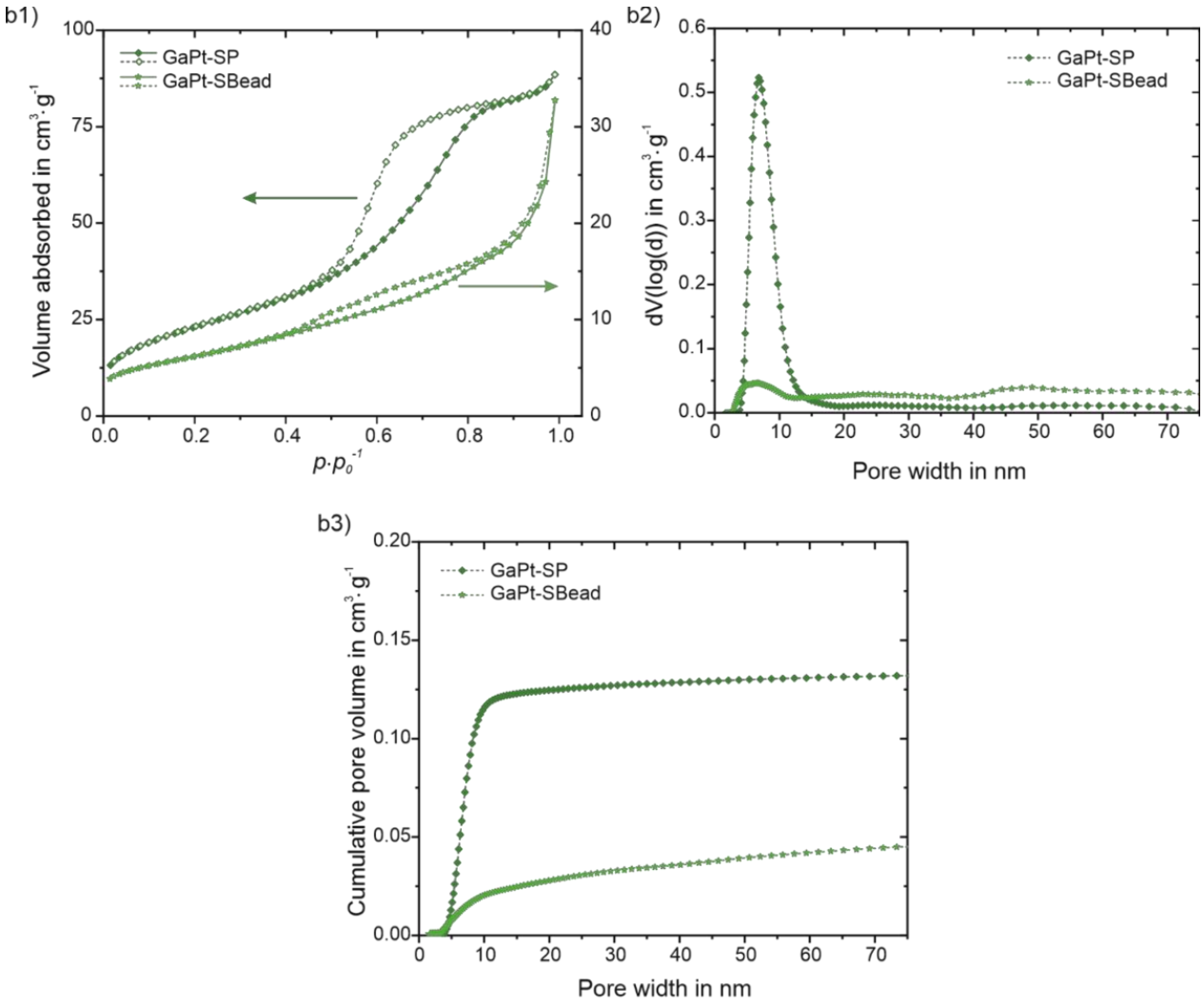

Figure S9: Pore system characterization of synthesized Ga_{130}Pt-SBeads in comparison with the corresponding Ga_{130}Pt-SP building block via N_2 sorption at 77 K. a) N_2 isotherms; full symbols represent the adsorption branch and empty symbols the desorption branch. b) Pore size distribution obtained by NLDFT. c) Cumulative pore volume as a function of pore width.

Table S3: Characteristic pore system values of synthesized SPs and the $Ga_{130}Pt$-SBeads (after synthesis; as prepared, after catalytic testing in reactor; spent) obtained from N_2 sorption analysis (Values in brackets are only shown to highlight changes of the pore system. Due to the absence of a plateau in the corresponding isotherms no accurate pore volume can be calculate).

Sample	S_{BET} / $m^2\ g^{-1}$	Total pore volume V_{pore} [a] / $cm^3\ g^{-1}$	Mean pore width $d_{mean\ pore}$ [b] / nm
SiO_2-SP	122	0.19	6.6
Pt-SP	101	0.17	6.6
Ga-SP	87	0.15	6.8
$Ga_{130}Pt$-SP	84	0.13	6.8
$Ga_{130}Pt$-SBead as prepared	23	(0.04)	6.6
$Ga_{130}Pt$-SBead spent	20	(0.03)	(43)

[a] obtained at $p \cdot p_0^{-1}$ of 0.97, [b] calculated via applying NLDFT method on the adsorption branch assuming a cylindrical pore shape.

The synthesized $Ga_{130}Pt$-SBeads display an isotherm consisting of a mixture of type II (overall shape of isotherm; typical for non and macroporous materials) and type IV (H2 type hysteresis between $p \cdot p_0^{-1}$ 0.4 and 0.8; typical for mesoporous materials).[R11] By applying NLDFT to the adsorption branch of the N_2 isotherms of $Ga_{130}Pt$-SBeads the pore size distribution and the cumulative pore volume were calculated. By comparing the PSD of the $Ga_{130}Pt$-SBeads with the PSD of the $Ga_{130}Pt$-SPs the influence of the mesopores of the SPs gets visible by the peak around 5 nm. For pore size values larger than 15 nm the influence of the macroporous/non-porous AlOx core gets visible by increased adsorbed N_2 amounts. These results support the findings from the SEM analysis of the Ga-SBeads (Figure 2) and the overall concept idea of mm-sized particles that are made of a macroporous/non-porous core material and a mesoporous species on top. The mesoporosity of the $Ga_{130}Pt$-SPs is still accessible for catalytic reaction after SBead fabrication.

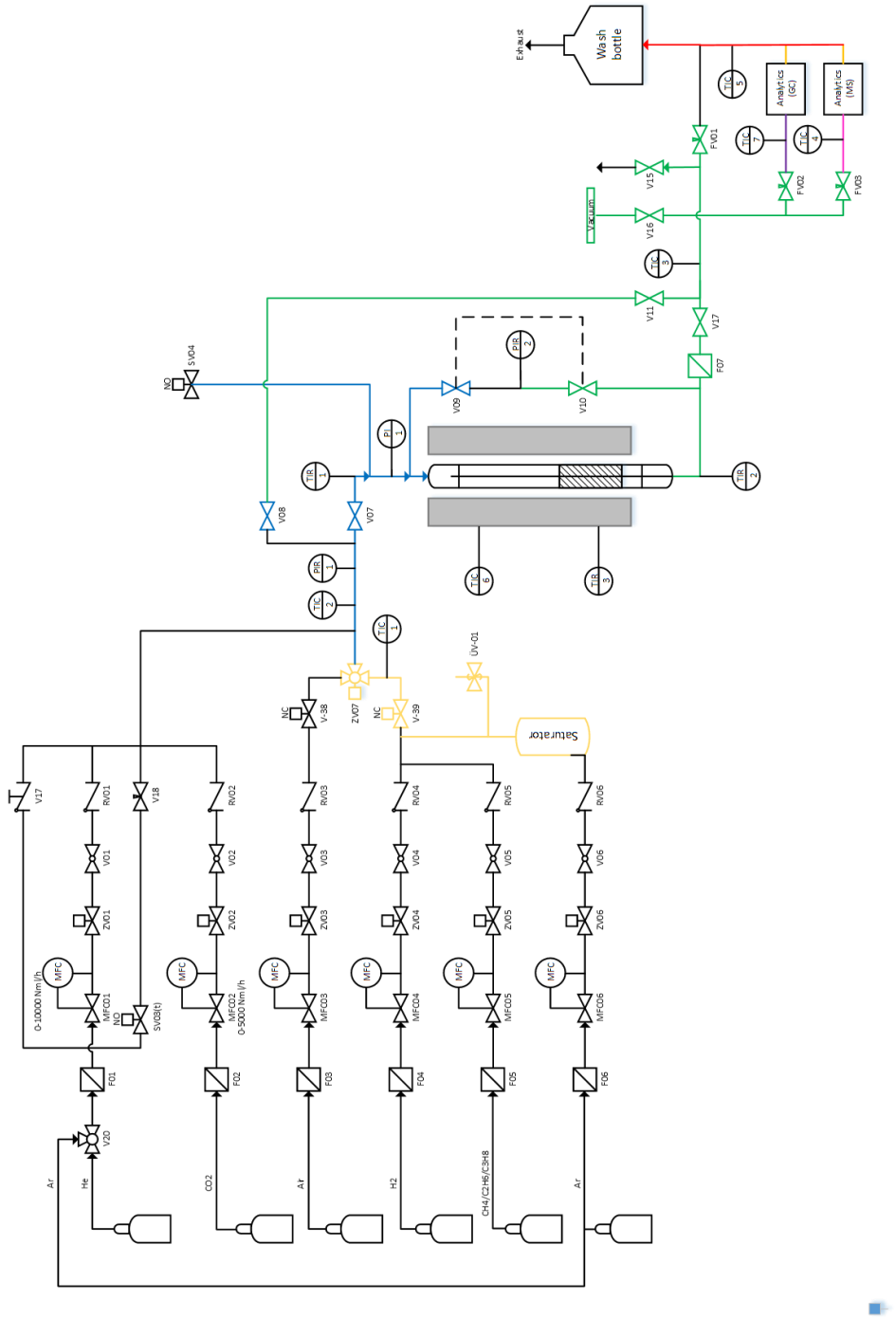

Figure S10. Flow scheme of the continuous gas-phase reactor used for propane dehydrogenation studies.

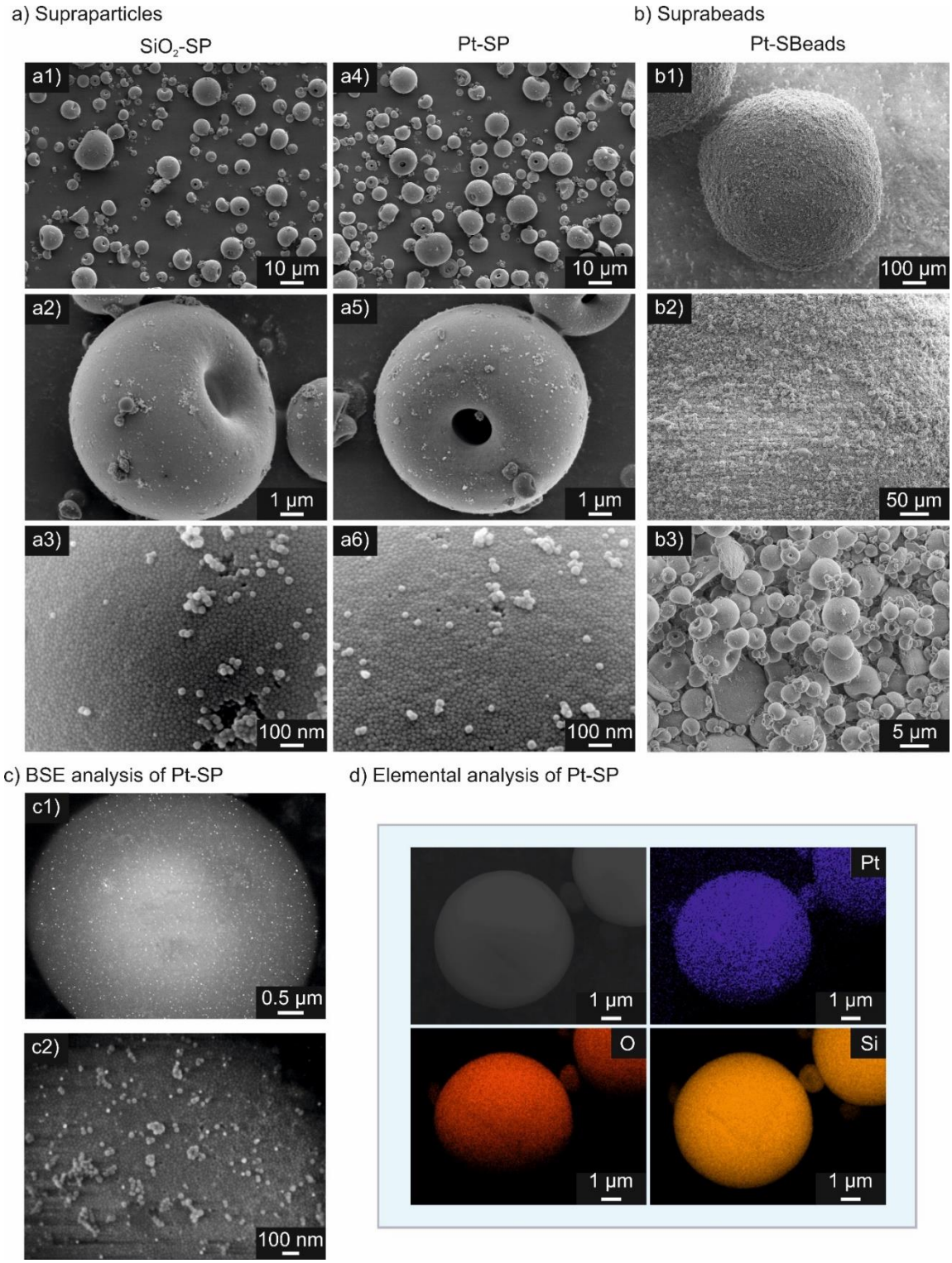

Figure S11: SEM of SiO_2-SP, with increasing magnifications from a1) to a3), as well as Pt-SP with increasing magnifications from a4) to a6), and Pt-SBead, with increasing magnifications from b1) to b3). c) shows the material contrast of the Pt-SP obtained from BSE-SEM analysis to highlight the Pt-distribution. d) elemental mapping of the Pt-SP

Propane dehydrogenation

Reference experiment: Further reference experiments of the bead and binder material was performed under same reaction conditions as the Ga-SBeads, Pt-SBeads and Ga_{130}Pt-SBeads-1 catalysts to confirm the absence of blind activity.

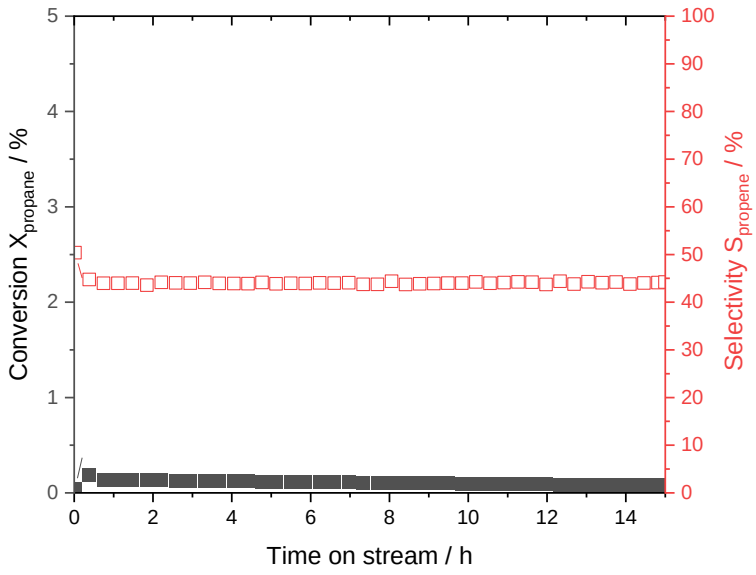

Figure S12. Conversion (filled symbols) and selectivity (open symbols) for blind activity using bead and binder in propane dehydrogenation. Catalyst mass in bed, 3 g. Pre-treatment conditions: 19.5 mL_N min^{-1} H_2, 80.5 mL_N min^{-1} Ar, 1.2 bar, 550 °C. PDH experiment: 8.9 mL_N min^{-1} C_3H_8, 89.9 mL_N min^{-1} Ar, 550 °C, 1.2 bar, 15 h TOS, GHSV: 1960 h^{-1}

Reproducibility experiment: To show good reproducibility in the synthesis and catalytic performance of the $Ga_{130}Pt$-SBeads-1, two additional samples were prepared using different batch of $Ga_{130}Pt$-SP. These new batches $Ga_{130}Pt$-SBeads-2 and $Ga_{130}Pt$-SBeads-3 were tested for catalytic activity under same conditions. The data on catalytic performance is provided in Figure S13.

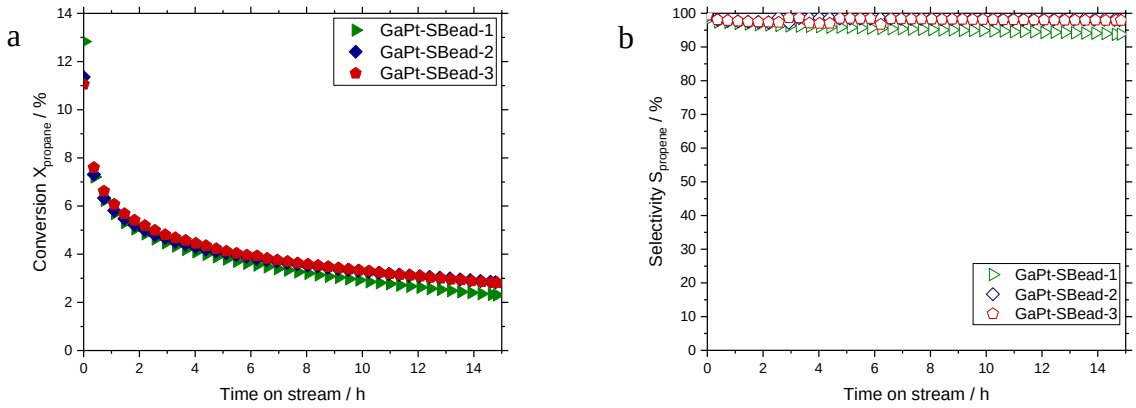

Figure S 13. Conversion (a; filled symbols) and selectivity (b; open symbols) of $Ga_{130}Pt$-SBead-1,2, and 3 in propane dehydrogenation. Catalyst mass in bed, 3 g. Pre-treatment conditions: 19.5 mL_N min^{-1} H_2, 80.5 mL_N min^{-1} Ar, 1.2 bar, 550 °C. PDH experiment: 8.9 mL_N min^{-1} C_3H_8, 89.9 mL_N min^{-1} Ar, 550 °C, 1.2 bar, 15 h TOS, GHSV: 1960 h^{-1}

Comparison of catalytic data of all catalysts tested:

Table S4: Catalytic propane dehydrogenation data for Ga-SBeads, Pt-SBeads, Ga_{130}Pt-SBeads-1 and the two reproductions of Ga_{130}Pt-SBeads.

Sample name	Ga wt%	Pt wt%	Ga/Pt $mol_{Ga}\ mol_{Pt}^{-1}$	X_0 %	S_0 %
Ga_{130}Pt-SBead-1	1.69	0.04	128	12.8	98.2
Ga_{130}Pt-SBead-2	1.08	0.02	132	11.3	98.2
Ga_{130}Pt-SBead-3	0.85	0.02	142	11.1	98.3
Ga-SBead	2.36	0	-	1.1	89.3
Pt-SBead	0	0.08	-	1.8	81.9
X_0 = initial conversion, S_0 = initial selectivity					

Comparison between $Ga_{45}Pt$ SCALMS and $Ga_{130}Pt$-SBeads: For comparison in catalytic performance with existing GaPt SCALMS systems, a traditional GaPt SCALMS catalysts was tested for catalytic activity under same conditions. The data on catalytic performance is provided in Figure S14.

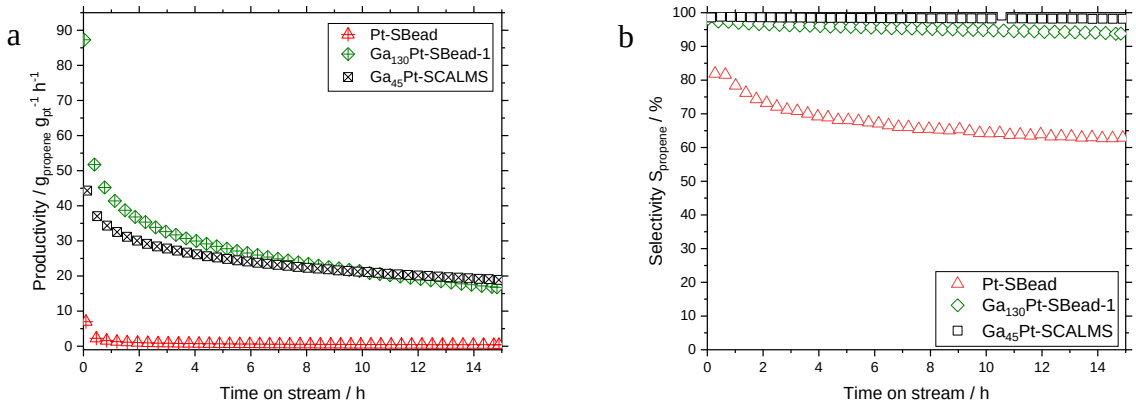

Figure S 14. Productivity (a; crossed symbols) and selectivity (b; open symbols) of Pt-SBeads (red), Ga_{130}Pt-SBead-1 (green), and Ga_{45}Pt SCALMS (black) in propane dehydrogenation. Pre-treatment conditions: 19.5 mL_N min^{-1} H_2, 80.5 mL_N min^{-1} Ar, 1.2 bar, 550 °C. PDH experiment: 8.9 mL_N min^{-1} C_3H_8, 89.9 mL_N min^{-1} Ar, 550 °C, 1.2 bar, 15 h TOS, GHSV: 1960 h^{-1}

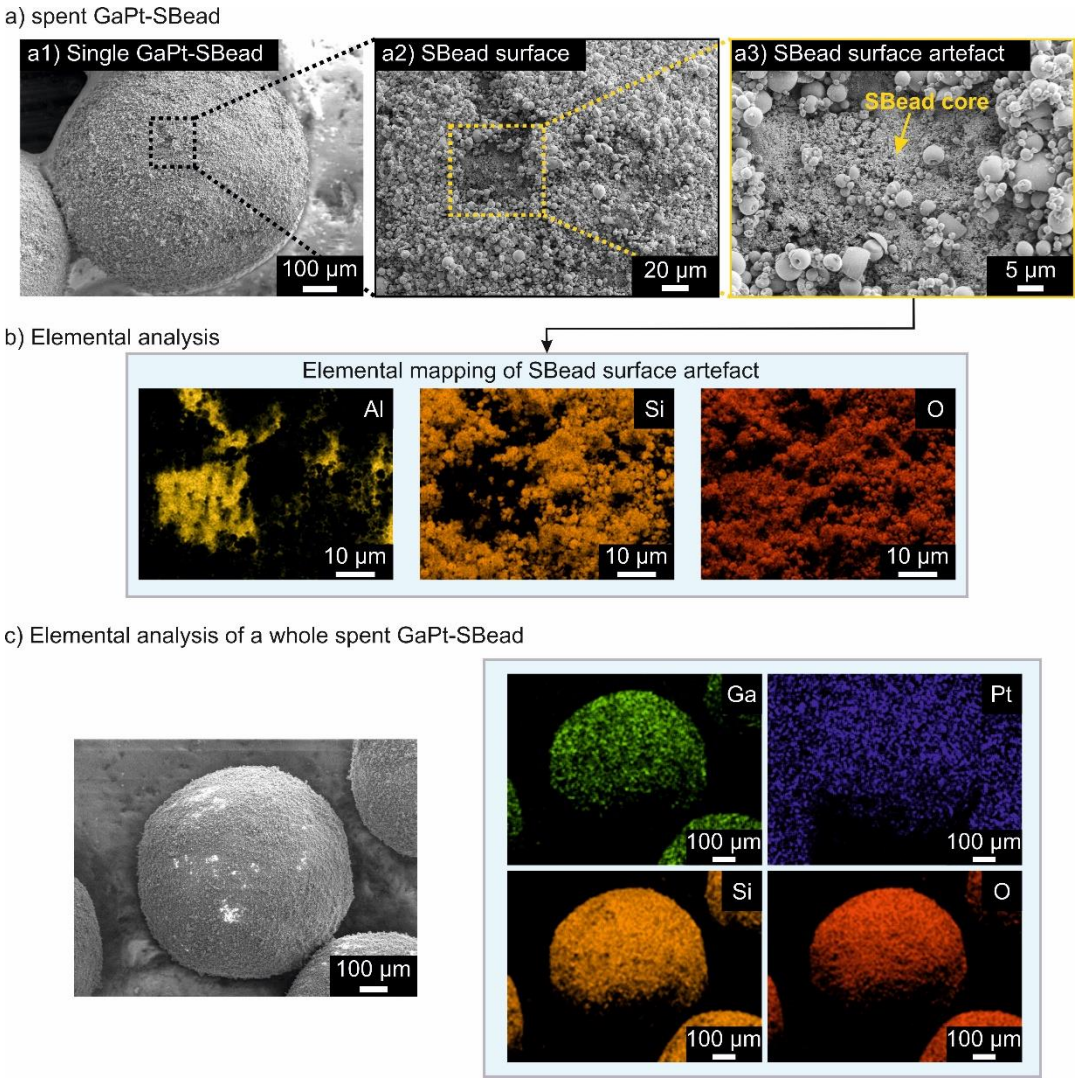

Figure S15: SEM of a) spent $Ga_{130}Pt$-SBead showing their surface with increasing magnifications from a1 to a3, as well as elemental mappings of it (b). c) displays the elemental distribution of Ga, Pt, Si, and O of the spent GaPt-SBeads after propane dehydrogenation. The homogeneous distribution after reaction indicates the immobilization of the catalytically active GaPt phase.

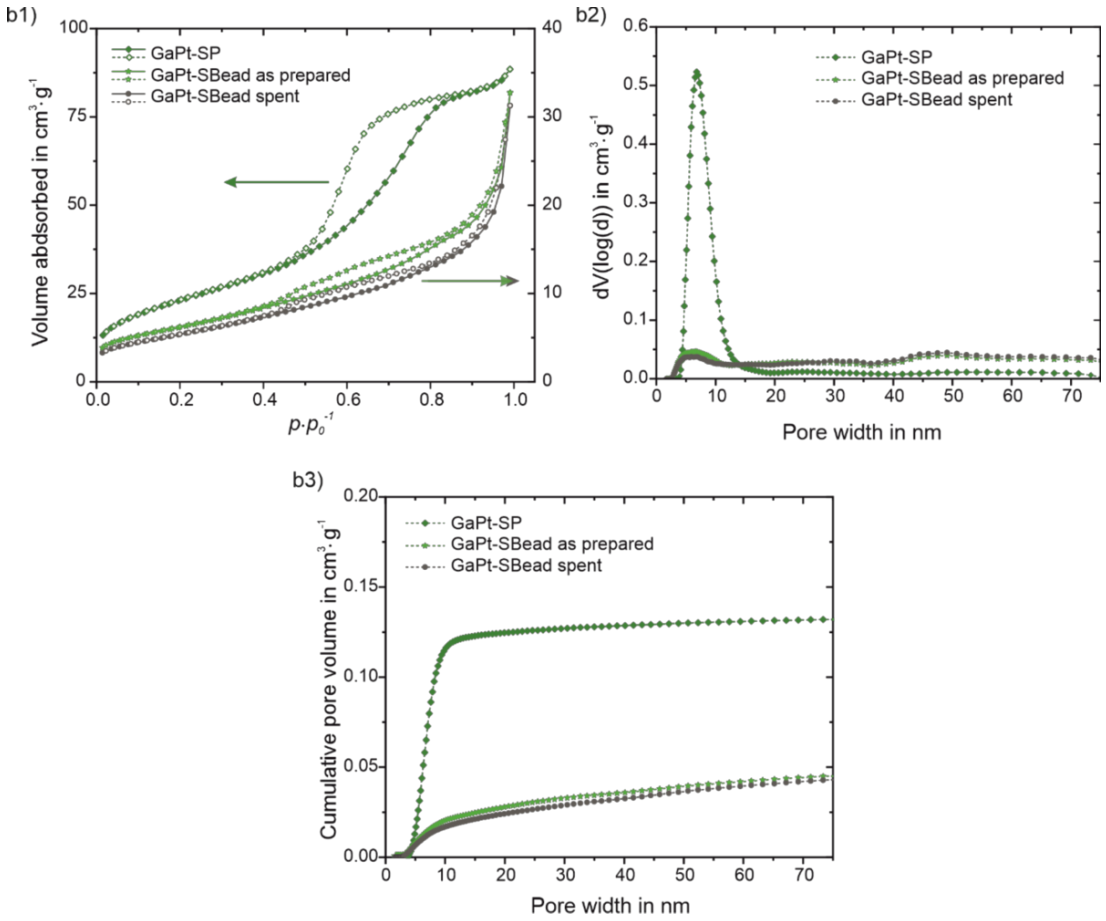

Figure S16. Pore system characterization of spent $Ga_{130}Pt$-SBeads in comparison with the corresponding $Ga_{130}Pt$-SBead before catalytic testing and the $Ga_{130}Pt$-SP building block via N_2 sorption at 77 K. a) N_2 isotherms; full symbols represent the adsorption branch and empty symbols the desorption branch. b) Pore size distribution obtained by NLDFT. c) Cumulative pore volume as a function of pore width.

N_2 sorption analysis of spent $Ga_{130}Pt$-SBeads reveal that pore system characteristics do not significantly change during reaction supporting the assumption of a sufficiently stabile SBead entity. For detailed discussion of the N_2 sorption isotherms, the PSD and the cumulative pore volume, as well as the characteristic values of the $Ga_{130}Pt$-SBead we refer to the discussion previously presented in this manuscript (Figure S9 and Table S3). The differences measured in absorbed N_2 volume can be attributed to slightly increased amount of surface artefacts on the $Ga_{130}Pt$-SBeads after reaction (compare Figure S16, SEM analysis of spent SBead).

Temperature programmed oxidation (TPO)

The spent catalyst and reference samples after PDH were analysed via temperature-programmed oxidation (TPO) in 21% O_2/He in order to determine the amount of coke formed during PDH. The weight change was observed using a high-resolution thermogravimetric analysis on a XEMIS sorption analyser (Hiden Isochema). A total of ~ 200 mg of the sample was placed in a cylindrical stainless steel mesh sample holder and heated to 500 °C (5 °C min-1) under He to remove both physisorbed and chemisorbed H20. After a hold time of 6 h, the sample was cooled down to 100 °C. The TPO experiment started by sending in a gas mixture of 21% O_2/He followed by a temperature increase to a maximum temperature of 500 °C (1 °C min^{-1}). The sample were held at this temperature for 12 h. The loss in mass relative to the original sample mass (m_{rel}) over the analysis time is shown in Figure S18.

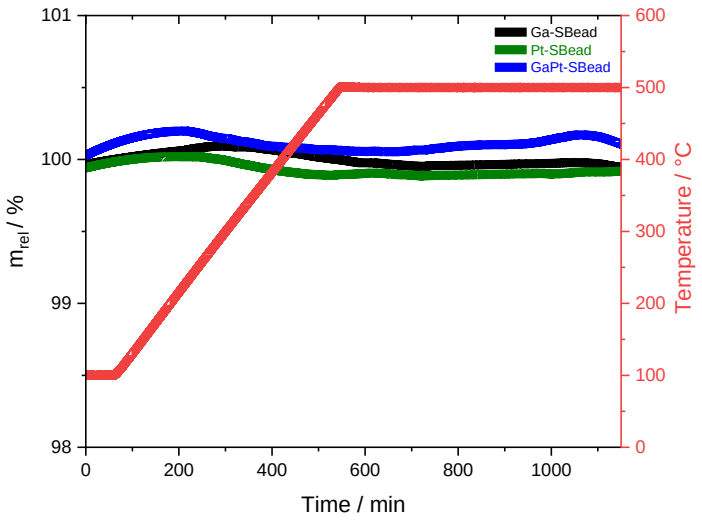

Figure S17. Sample weight relative to the weight prior to exposure to 21% O2/He at 100 °C during temperature-programmed oxidation of spent Ga-SBeads (black), Pt-SBeads (green) and Ga_{130}Pt-Sbead-1 (blue). These catalyst systems were investigated after propane dehydrogenation at 550 °C as monitored via high-resolution thermogravimetry. Conditions: 0.2 g spent catalyst, 1 °C min^{-1}, p_{total} =1 bar, He = 100 mL_N min^{-1} He (TOS < 0); 79 mL_N min^{-1} He and 21 mL_N min^{-1} O_2 (TOS > 0)

ESI Video 1: HRES PC nano-CT tilt series (supraparticles as prepared)

ESI Video 2: Virtual reconstructed slices of HRES PC nano-CT tilt series

ESI Video 3: 3D visualization of HRES PC nano-CT tilt series

ESI References:

R1 *Germany Pat.*, C09J 1/000 (2006.01), 2010.

R2 Wang, J.; Chen, Y.-c.K.; Yuan, Q.; Tkachuk, A.; Erdonmez, C.; Hornberger, B.; Feser, M. Automated markerless full field hard x-ray microscopic tomography at sub-50 nm 3-dimension spatial resolution. *Appl Phys Lett* 2012, **100**, 143107.

R3 Gilbert, P. Iterative methods for the three-dimensional reconstruction of an object from projections. *J. Theor. Biol.* 1972, **36**, 105-117.

R4 van Aarle, W.; Palenstijn, W.J.; De Beenhouwer, J.; Altantzis, T.; Bals, S.; Batenburg, K.J.; Sijbers, J. The ASTRA Toolbox: A platform for advanced algorithm development in electron tomography. *Ultramicroscopy* 2015, **157**, 35-47.

R5 R5 M. D. Dickey, Emerging applications of liquid metals featuring surface oxides, *ACS applied materials & interfaces*, 2014, **6**, 18369–18379.

R6 J. Yan, Y. Lu, G. Chen, M. Yang and Z. Gu, Advances in liquid metals for biomedical applications, *Chemical Society Reviews*, 2018, **47**, 2518–2533.

R7 F. Iskandar, L. Gradon and K. Okuyama, Control of the morphology of nanostructured particles prepared by the spray drying of a nanoparticle sol, *Journal of Colloid and Interface Science*, 2003, **265**, 296–303.

R8 A. B. D. Nandiyanto, T. Ogi, W.-N. Wang, L. Gradon and K. Okuyama, Template-assisted spray-drying method for the fabrication of porous particles with tunable structures, *Advanced Powder Technology*, 2019, **30**, 2908–2924.

R9 A. B. D. Nandiyanto, T. Ogi, W.-N. Wang, L. Gradon and K. Okuyama, Template-assisted spray-drying method for the fabrication of porous particles with tunable structures, *Advanced Powder Technology*, 2019, **30**, 2908–2924.

R10 S. Zellmer, G. Garnweitner, T. Breinlinger, T. Kraft and C. Schilde, Hierarchical Structure Formation of Nanoparticulate Spray-Dried Composite Aggregates, *ACS nano*, 2015, **9**, 10749–10757.

R11 M. Thommes, K. Kaneko, A. V. Neimark, J. P. Olivier, F. Rodriguez-Reinoso, J. Rouquerol and K. S. Sing, Physisorption of gases, with special reference to the evaluation of surface area and pore size distribution (IUPAC Technical Report), *Pure and Applied Chemistry*, 2015, **87**, 1051–1069.

R12 M. Thommes, B. Smarsly, M. Groenewolt, P. I. Ravikovitch and A. V. Neimark, Adsorption hysteresis of nitrogen and argon in pore networks and characterization of novel micro- and mesoporous silicas, *Langmuir*, 2006, **22**, 756–764.

R13 J. Landers, G. Y. Gor and A. V. Neimark, Density functional theory methods for characterization of porous materials, *Colloids and Surfaces A: Physicochemical and Engineering Aspects*, 2013, **437**, 3–32.